Published in final edited form as:
J Heat Transfer. 2010 November 1; 132(11): 1–9.

An Experimentally Validated Numerical Modeling Technique for Perforated Plate Heat Exchangers

M. J. White,
Accelerator Division/Cryogenic Systems, Fermi National Accelerator Laboratory, Batavia, IL 60510

G. F. Nellis,
Department of Mechanical Engineering, University of Wisconsin-Madison, Madison, WI 53703

S. A. Kelin,
Department of Mechanical Engineering, University of Wisconsin-Madison, Madison, WI 53703

W. Zhu, and
Department of Mechanical Engineering, University of Michigan-Ann Arbor, Ann Arbor, MI 48109

Y. Gianchandani
Department of Mechanical Engineering, University of Michigan-Ann Arbor, Ann Arbor, MI 48109

Abstract

Cryogenic and high-temperature systems often require compact heat exchangers with a high resistance to axial conduction in order to control the heat transfer induced by axial temperature differences. One attractive design for such applications is a perforated plate heat exchanger that utilizes high conductivity perforated plates to provide the stream-to-stream heat transfer and low conductivity spacers to prevent axial conduction between the perforated plates. This paper presents a numerical model of a perforated plate heat exchanger that accounts for axial conduction, external parasitic heat loads, variable fluid and material properties, and conduction to and from the ends of the heat exchanger. The numerical model is validated by experimentally testing several perforated plate heat exchangers that are fabricated using microelectromechanical systems based manufacturing methods. This type of heat exchanger was investigated for potential use in a cryosurgical probe. One of these heat exchangers included perforated plates with integrated platinum resistance thermometers. These plates provided in situ measurements of the internal temperature distribution in addition to the temperature, pressure, and flow rate measured at the inlet and exit ports of the device. The platinum wires were deposited between the fluid passages on the perforated plate and are used to measure the temperature at the interface between the wall material and the flowing fluid. The experimental testing demonstrates the ability of the numerical model to accurately predict both the overall performance and the internal temperature distribution of perforated plate heat exchangers over a range of geometry and operating conditions. The parameters that were varied include the axial length, temperature range, mass flow rate, and working fluid.

Keywords

perforated plate; heat exchanger; axial conduction; cryogenic; MEMS

Correspondence to: M. J. White.

Contributed by the Heat Transfer Division of ASME for publication in the JOURNAL OF HEAT TRANSFER.

1 Introduction

Perforated plate heat exchangers were invented in the 1940s by McMahon et al. [1] and are often used to provide a compact design for a recuperative heat exchanger in applications where high effectiveness is required in the presence of a large operating temperature span. A perforated plate heat exchanger is constructed of many plates that are oriented perpendicular to the flow. Two different types of plates are used in an alternating sequence. Low conductivity spacers provide a high axial resistance and the perforated plates provide a high stream-to-stream conductance to create a compact heat exchanger. The plates are hermetically sealed to prevent fluid leakage between the streams and to the external environment. Figure 1 illustrates, qualitatively, the temperature distribution expected in the fluids and the spacer/heat transfer plate material [2].

The perforated plates are composed of high conductivity material and include many small flow passages. Therefore, the stream-to-stream thermal resistance within the heat exchanger plate is low. The spacer is made of low conductivity material and the cross-sectional area available for axial conduction in each spacer is small. Therefore, the temperature gradient across each spacer is approximately linear. The fluid passing through the spacer does not change temperature significantly because there is very little surface area for heat transfer and therefore the stream-to-stream thermal communication is poor.

Perforated plate heat exchangers have been used as the recuperative heat exchanger for cryogenic refrigerators. For example, perforated plate heat exchanger consisting of copper heat transfer plates interspersed with stainless steel spacers have been used in turbo-Brayton cryocooler for space applications [3]. Jeheon and Jeong [4] discussed a perforated plate heat exchanger fabricated from copper plates separated by Kapton spacers. Venkatarathnam and Sarangi [5] presented a review of perforated plate heat exchangers and their manufacture and application.

Modeling of perforated plate heat exchangers is often accomplished by ignoring the discrete nature of the plate-spacer structure of the heat exchanger in order to treat the plates as a series of fins. This approach ignores the impact of the discrete plates that is clearly evident in Fig. 1 as well as the effect of axial conduction. For high effectiveness applications, these effects can dominate the performance of the heat exchanger. Venkatarathnam [6] derived the closed form effectiveness-*NTU* solution for a perforated plate heat exchanger. However, the use of this solution necessarily neglects the effect of temperature-dependent properties and does not explicitly include the effect of axial conduction. Several researchers have examined the impact of axial conduction on continuous heat exchangers, for example, Refs. [7–10]. More detailed numerical models of perforated plate heat exchanger models simulate each plate-spacer pair individually and integrate these solutions using energy balances. Examples of this approach include Refs. [11–13].

The numerical model presented in this paper is an example of this approach. The detailed heat exchanger numerical model previously published by Nellis [8] in order to understand the impact of axial conduction and parasitic heat load is used to simulate each individual plate. The model was expanded in order to allow a specified heat transfer rate at each end. The models of individual plates are integrated via energy balances in order to develop a detailed numerical model of the entire perforated plate heat exchanger.

The model was specifically applied to a perforated plate heat exchanger with silicon heat transfer plates and borosilicate glass spacers that was manufactured using microelectromechanical systems (MEMS)-based processes. The heat exchanger was instrumented and installed in a vacuum test facility for performance testing. One advantage of MEMS-based manufacturing is that it is possible to integrate various types of sensors with the

plates. Some of the tested perforated plate heat exchangers included platinum resistance thermometers (PRTs) integrated with individual plates, allowing the resolution of the internal details of the heat exchanger processes. These integrated PRTs provide the only direct and internal verification of a perforated plate heat exchanger model that the authors are aware of and clearly show interesting behavior such as the temperature-jump phenomena that is expected for heat exchangers experiencing a large amount of axial conduction. Other researchers (for example, Refs. [13,14]) have compared the overall performance (e.g., heat transfer rate or effectiveness) with model prediction but have not measured and compared the internal temperature distribution.

Section 1 describes the numerical model of a single plate. Section 2 describes the energy balances that are necessary to integrate the single-plate models and models of the spacers in order to develop a set of equations that describe the thermal behavior of the entire heat exchanger. The implementation of these equations in the iterative equation solver EES [15] is discussed. Section 5 presents the experimental measurements that are used to validate the numerical model, including in situ measurements of the temperature distribution within the heat exchanger.

2 Single-Plate Heat Exchanger Model

The model of a single heat exchanger plate is based on the numerical simulation technique developed by Nellis [8]. Figure 2 illustrates a schematic of a single plate, which experiences a flow of hot fluid on one side (entering at $T_{h,\text{in}}$ with total capacitance rate $\dot{C}_h$) and cold fluid on the other (entering at $T_{c,\text{in}}$ with total capacitance rate $\dot{C}_c$) as well as an external and parasitic heat transfer to the hot fluid ($\dot{q}_h$) and the cold fluid ($\dot{q}_c$) along the length of the plate and into either end of the plate ($\dot{q}_{w,h}$ and $\dot{q}_{w,c}$). Within any single plate, the properties of the working fluid and material are assumed to be temperature independent, but they may vary from plate to plate.

The model is developed in dimensionless form in order to maximize its utility and modularity. The dimensionless temperatures of the hot fluid (θ_h), cold fluid (θ_c), and wall (θ_w) are defined according to

$$\theta = \frac{T - T_{c,\text{in}}}{T_{h,\text{in}} - T_{c,\text{in}}} \tag{1}$$

The axial conduction parameter λ is the dimensionless parameter that captures the relative importance of axial conduction within the plate (not across the entire heat exchanger). The axial conduction parameter is approximately equal to the ratio of the heat conducted axially to the heat conducted stream-to-stream and it is defined according to [7]

$$\lambda = \frac{1}{R_{\text{ac}}\dot{C}_{\min}} \tag{2}$$

where R_{ac} is the thermal resistance to axial conduction through the plate and $\dot{C}_{\min}$ is the minimum capacitance rate. The dimensionless parasitic heat loads along the length of the plate (χ_h and χ_c) and into the ends of the plate ($\chi_{w,h}$ and $\chi_{w,c}$) are defined by normalizing against the maximum possible rate of heat transfer:

$$\chi = \frac{\dot{q}}{\dot{C}_{\min}(T_{h,\text{in}} - T_{c,\text{in}})} \tag{3}$$

The dimensionless capacitance rates of the hot and cold fluid are defined as

$$\mu=\frac{\dot{C}_h}{\dot{C}_{\min}} \tag{4}$$

$$\upsilon=\frac{\dot{C}_c}{\dot{C}_{\min}} \tag{5}$$

The total number of transfer units on either side of the plate (NTU_h and NTU_c) is defined as the ratio of the conductance between the stream and the plate (UA_h and UA_c) to the minimum capacity rate ($\dot{C}_{\min}$).

$$NTU_h=\frac{UA_h}{\dot{C}_{\min}} \tag{6}$$

$$NTU_c=\frac{UA_c}{\dot{C}_{\min}} \tag{7}$$

The conductance must include the convective heat transfer between the fluid and the surface as well as conduction resistance within the plate.

Each plate is modeled using a numerical model based on a finite difference technique. Figure 3 illustrates the distribution of the nodes within the plate.

The dimensionless axial distance from the hot end of the plate (Z) is defined according to

$$Z=\frac{x}{L} \tag{8}$$

where x is the axial distance from the hot end of the plate and L is the total thickness of the plate. The dimensionless width of an individual element is

$$\Delta Z=\frac{\Delta x}{L} \tag{9}$$

where Δx is the dimensional width of the element. The computational efficiency of the numerical model is increased by using an exponentially distributed grid of nodes in order to allow the elements to be concentrated toward the ends of the plate. The width of an individual element ΔZ_i is calculated using

$$\Delta Z_i=\frac{\exp(-\gamma(1-2i/N))}{2\Sigma_{i=1}^{N/2}\exp(-\gamma(1-2i/N))} \tag{10}$$

where N is the number of elements and γ is the grid concentration factor. If the grid concentration factor γ is equal to 0, then the grid is equally distributed across the length of the

heat exchanger. Positive values of γ result in the elements being concentrated near the heat exchanger ends and negative values result in the elements being concentrated in the middle of the heat exchanger.

The dimensionless hot side energy balance for an arbitrary *i*th segment is given by

$$\mu_h\theta_{h,i-1}+\chi_h\Delta Z_i=\mu_h\theta_{h,i}+NTU_h\Delta Z_i\left(\frac{\theta_{h,i}+\theta_{h,i-1}}{2}-\theta_{w,i}\right)\ \text{for}\ i=1,\ldots,N \tag{11}$$

The dimensionless cold side energy balance for an arbitrary *i*th segment is

$$\chi_c\Delta Z_i+\upsilon_c\theta_{c,i}+NTU_c\Delta Z_i\left(\theta_{w,i}-\frac{\theta_{c,i}+\theta_{c,i-1}}{2}\right)=\upsilon_c\theta_{c,i-1}\ \text{for}\ i=1,\ldots,N \tag{12}$$

The dimensionless wall energy balance for an arbitrary *i*th segment is

$$\begin{aligned}\chi_w\Delta Z_i+NTU_h\Delta Z_i\left(\frac{\theta_{h,i}+\theta_{h,i-1}}{2}-\theta_{w,i}\right)+\frac{2\lambda}{\Delta Z_i+\Delta Z_{i-1}}(\theta_{w,i-1}-\theta_{w,i})\\ =NTU_c\Delta Z_i\left(\theta_{w,i}-\frac{\theta_{c,i}+\theta_{c,i-1}}{2}\right)+\frac{2\lambda}{\Delta Z_i+\Delta Z_{i+1}}(\theta_{w,i}-\theta_{w,i+1})\ \text{for}\ i=2\cdots(N-1)\end{aligned} \tag{13}$$

The wall elements at the ends of the heat exchanger must be treated separately. The energy balances on the first and last segments are

$$\begin{aligned}\chi_w\Delta Z_1+NTU_h\Delta Z_1\left(\frac{\theta_{h,1}+\theta_{h,0}}{2}-\theta_{w,1}\right)+\frac{\lambda}{\Delta Z_0}(\theta_{w,0}-\theta_{w,1})\\ =NTU_c\Delta Z_i\left(\theta_{w,1}-\frac{\theta_{c,1}+\theta_{c,0}}{2}\right)+\frac{2\lambda}{\Delta Z_1+\Delta Z_2}(\theta_{w,1}-\theta_{w,2})\end{aligned} \tag{14}$$

$$\begin{aligned}NTU_h\Delta Z_N\left(\frac{\theta_{h,N}+\theta_{h,N-1}}{2}-\theta_{w,N}\right)+\chi_w\Delta Z_N+\frac{2\lambda}{\Delta Z_N+\Delta Z_{N-1}}(\theta_{w,N-1}-\theta_{w,N})\\ =NTU_c\Delta Z_N\left(\theta_{w,N}-\frac{\theta_{c,N}+\theta_{c,N-1}}{2}\right)+\frac{\lambda}{\Delta Z_{N+1}}(\theta_{w,N}-\theta_{w,N+1})\end{aligned} \tag{15}$$

Four boundary conditions are required to complete the set of algebraic equations. Two boundary conditions are defined by the fluid inlet temperatures:

$$\theta_{h,i=0}=1 \tag{16}$$

$$\theta_{c,i=N}=0 \tag{17}$$

The wall end conduction boundary equations are

$$\theta_{w,i=0}=\frac{\chi_{w,h}\Delta Z_0}{\lambda}+\theta_{w,i=1} \tag{18}$$

$$\theta_{w,i=N}=\frac{\chi_{w,c}\Delta Z_{N+1}}{\lambda}+\theta_{w,i=N+1} \tag{19}$$

The numerical model is implemented as a subprogram in EES [15]. The subprogram requires the dimensionless characteristics of the plate and inlet conditions; it returns the dimensionless outlet fluid temperatures ($\theta_{h,\text{out}}$ and $\theta_{c,\text{out}}$) as well as the dimensionless temperature of the wall material at the hot and cold ends ($\theta_{w,h}$ and $\theta_{w,c}$). These values can be used to compute the outlet fluid temperatures ($T_{h,\text{in}}$ and $T_{c,\text{in}}$) and hot and cold end wall temperatures ($T_{w,h}$ and $T_{w,c}$).

3 Integration of the Single-Plate Heat Exchanger Models

The perforated plate heat exchanger is modeled as a series of constant property heat exchangers (one per plate) using the single-plate heat exchanger model described in Sec. 2. The plates and spacers are integrated, as shown in Fig. 4.

The thermodynamic and transport properties of the fluid and material are evaluated using the temperatures and pressures at the axial midpoint of each perforated plate. The numerical model described with an exponentially distributed grid (the concentration factor is set to $\gamma = 1.5$) provides the temperature distribution within each plate and the outlet temperatures. This approach of separately simulating each plate using a detailed numerical model allows for accurate estimates of the temperature distribution with modest computational effort.

The surface area of the spacers is so small (28 mm^2 versus 430 mm^2) and the thermal conductivity is so small relative to the perforated plates (less than 1.3 W/m K for glass versus greater than 150 W/m K for silicon) that the stream-to-stream heat transfer in the spacers can be neglected. This is a conservative assumption as any small additional heat transfer that occurs between the plates will improve the heat exchanger performance. However, the quantity of heat that is conducted axially through each spacer into the adjacent heat exchanger plate cannot be neglected. Figure 4 shows the numbering system used to integrate the plate and spacer models.

The plate and spacer models are integrated as follows. For an arbitrary plate j, the hot fluid inlet temperature is taken to be the hot fluid outlet temperature of plate $j-1$ (i.e., no energy transfer occurs as the fluid passes through the spacer). Similarly, the cold fluid inlet temperature is taken to be the cold fluid outlet temperature of plate $j+1$. The hot fluid inlet temperature for the first plate (plate 1) is the temperature of the hot fluid entering the device. The cold fluid inlet temperature for the last plate (plate N_p) is the temperature of the cold fluid entering the device. The ends of the perforated plate heat exchanger are assumed to be insulated. Therefore, $\dot{q}_{w,h,1}$ and $\dot{q}_{w,c,Np}$ are both zero. The rates of heat transfer into the ends of each plate are related to the end temperatures according to the resistance of the spacers:

$$\dot{q}_{w.c,j}=\dot{q}_{w,h,j+1}=\frac{(T_{w,c,j}-T_{w,h,j+1})}{R_{\text{sp},j}} \text{ for } j=1,\ldots,N_p \tag{20}$$

where R_{sp} is the thermal resistance of the spacer, also computed at the average temperature of the spacer.

The calculation of the plate conductance and plate and spacer thermal resistances as well as the parasitic heat loads all depend on the specific geometry and materials used to construct the perforated plate heat exchanger and the fluid properties. In general, user-specific functions must be written in order to account for the geometry, materials, and working fluids for the particular heat exchanger being studied. Further details about the numerical model as well as a discussion of the specific calculations used to model the experimental perforated plate heat exchanger that is presented in this paper are presented in Ref. [16].

The solution to the set of implicit nonlinear equations required to simulate the perforated plate heat exchanger is facilitated by the use of the iterative equation solver EES [15] and a set of reasonable initial guess values. Because of the nonlinear character of the equations related to the temperature-dependent properties, the model has a low probability of convergence unless a systematic approach is used to provide reasonable guess values for the iteration process. The following guidelines are used to develop a set of guess values that will allow the equation solver to reliably converge on a solution.

A linear temperature distribution is assumed and used as guess values for the wall and fluid streams and a constant fluid pressure is assumed for each stream. In addition, all thermophysical properties should initially be set by the user to constant values consistent with the average value of these quantities. If parasitic heat loads exist, they should initially be set to zero. If a small number of plates are chosen, the model should converge on a solution very quickly in this limit. The number of plates (N_p) should be gradually increased (after the guess values are updated) until the desired number of plates is reached. The number of segments used to simulate each perforated plate (N) should be kept low (between 4 and 8) during this step in order to reduce computational time. The results from the previous solution should always be used as the guess values for the next solution in order to optimize convergence time and reliability. The next step is to adjust the number of segments used to simulate each perforated plate. The number of segments required is dependent on the accuracy required and the temperature differences (stream-to-stream and axial). As a general rule, the number of nodes should be increased until the stream outlet temperatures remain constant to within a desired accuracy. The user-specific material and fluid property functions with the largest impact on the temperature distribution and the most variability across the entire heat exchanger should be included into the numerical model first, after updating guess values based on the constant property solution. In refrigeration applications, the working fluid is generally at or near the liquefaction temperature near the cold end of the heat exchanger and therefore the fluid properties are often more important and more temperature dependent than the material properties. Usually, it is best to activate temperature-dependent fluid heat capacity first, followed by the axial and stream-to-stream thermal resistances and then the pressure drop, and parasitic heat load calculations.

These guidelines were found to be useful in the process of modeling the cryogenic heat exchanger discussed in Sec. 4. Different applications may require a re-ordering of the sequence in which variables are switched from constant to temperature dependent. In addition, some applications may allow some of the above steps to be performed in parallel, while other applications may require the activation of temperature-dependent properties one stream at a time.

The effectiveness of the heat exchanger is the primary output of the model as is defined as the ratio of the actual rate of heat transfer to the maximum possible rate of heat transfer. Due to the presence of parasitic heat transfer, the effectiveness may be defined using either the rate of heat transfer from the hot fluid or to the cold fluid:

$$\varepsilon_h = \frac{\dot{m}_h(i_{h,T=T_{h,\text{in}}} - i_{h,T=T_{h,\text{out}}})}{\dot{q}_{\max}} \tag{21}$$

$$\varepsilon_c = \frac{\dot{m}_c(i_{c,T=T_{c,\text{out}}} - i_{c,T=T_{c,\text{in}}})}{\dot{q}_{\max}} \tag{22}$$

where i is the mass specific enthalpy, $\dot{m}$ is the mass flow rate, and $\dot{q}_{\max}$ is the maximum possible rate of heat transfer. The maximum possible rate of heat transfer is defined as the minimum of the rate of heat transfer required to bring the hot fluid to the cold fluid inlet temperature and the rate of heat transfer required bring the cold fluid to the hot fluid inlet temperature:

$$\dot{q}_{\max} = \min[\dot{m}_c(i_{c,T=T_{h,\text{out}}} - i_{c,T=T_{c,\text{in}}}), \dot{m}_h(i_{h,T=T_{h,\text{in}}} - i_{h,T=T_{c,\text{in}}})] \tag{23}$$

4 Experimental Validation

An experimental test facility was constructed with commercially calibrated PRTs in order to measure the performance of small perforated plate heat exchangers for cryogenic applications. A schematic of the facility is shown in Fig. 5.

The warm inlet temperature to the heat exchanger was maintained near room temperature (295 K) and the cold inlet temperature to the heat exchanger was controlled by the use of a cryocooler and heater. The heat exchanger was tested inside a large vacuum insulated container with multilayer insulation (MLI) so that parasitic heat loads could be minimized. The hot side inlet pressure was kept at approximately 2 bar absolute or lower and the cold side outlet pressure was kept slightly above 1 bar absolute. The numerical model results showed a low sensitivity to pressure drop. Further information on the calculated and experimental pressure profiles, which are unique for each heat exchanger, can be found in Ref. [16].

The heat exchangers that were tested were designed for a cryosurgical application. The objective was to create a lightweight and compact heat exchanger that could be installed in the part of a cryoprobe that is held in a surgeon's hand. The perforated plates were fabricated from silicon, which has a high thermal conductivity (similar to that of copper). The spacers were fabricated from borosilicate glass, which has a low thermal conductivity (less than that of stainless steel). Silicon and borosilicate glass were selected not only because of their desirable material properties but also because they are nonmagnetic (and therefore MRI compatible) and can be manufactured using existing MEMS equipment and procedures. A MRI compatible cryoprobe has the potential to provide the surgeon with real-time feedback related to the size and shape of the frozen tissue, which will allow complete ablation of the malignant tissue to be verified. Utilizing MEMS-fabrication technology may allow the use of many, small-scale, highly engineered flow passages in the heat exchanger plate.

The silicon and borosilicate glass were anodically bonded at the wafer level and diced in order to form "dies," which consist of one perforated plate and one glass spacer. The outer dimensions of the die are $10 \times 10\ \text{mm}^2$. For each stream there are two columns of 74 flow passages installed in the perforated plate. The flow passages each have a cross section of $1.4 \times 0.05\ \text{mm}^2$ and the thickness of the silicon plate is 0.5 mm. The glass spacers had a thickness of 0.3 mm. The dies were stacked and bonded using a common cryogenic epoxy. Stainless steel headers are attached

with epoxy to the heat exchanger stack in order to provide the interface between the heat exchanger and the experimental test facility.

One of the prototype heat exchangers contained perforated plates with platinum wires deposited on the surface to provide integrated temperature sensors [17]. The platinum wires were deposited on the fin material that was between the micromachined ducts. Because of the low contact resistance between the PRT and the wall, the temperature measured by the PRTs is biased toward the duct wall temperature rather than the actual fluid temperature. Thus the hot side integrated PRT measurements will be biased slightly lower and the cold side PRT measurements will be biased slightly higher than the actual fluid temperature. Figure 6(*a*) illustrates a single die with an integrated PRT with measurement leads. Figure 6(*b*) illustrates a perforated plate heat exchanger composed of several plate/spacer dies. Figure 6(*c*) illustrates the perforated plate heat exchanger integrated with headers. More information regarding the design and fabrication of the heat exchanger and the experimental test facility can be found in the literature [16,18–21].

The first prototype heat exchanger that was tested consisted of 16 dies and contained no integrated PRTs. The heat exchanger was tested using helium gas over a range of mass flow rate. The warm inlet temperature was maintained between 299 K and 301 K, while the cold inlet temperature was maintained between 196 K and 207 K. All heat exchanger inlet and outlet temperatures were measured using commercially calibrated PRTs with a rated absolute uncertainty of ±0.25 K. Figure 7 illustrates the measured effectiveness based on the hot and cold streams as well as the predicted values of these quantities as a function of mass flow rate. The details related to the calculation of the experimental uncertainty can be found in Ref. [16].

The numerical model predictions are within the experimental uncertainty over the entire range of flow rates measured. The numerical model was always solved starting with two elements for each plate. The number of elements per plate was increased by two until two consecutive solutions had outlet temperatures identical to within ±0.01 K, which generally was eight elements per plate for the plots shown in this paper.

A similar test was performed on a heat exchanger that consists of 43 dies and these results are shown in Fig. 8. The warm inlet temperature was maintained between 295 K and 303 K and the cold inlet temperature was maintained between 237 K and 252 K for these tests. The predicted effectiveness lies slightly out of the range of experimental uncertainty range for a few data points but is within the experimental uncertainty for the majority of the points. Also overlaid onto Fig. 8 are the 16 die effectiveness test results from Fig. 7. The 43 die heat exchanger exhibited a significantly higher effectiveness over the entire range of flow rates tested. This is expected as the 43 die heat exchanger has both a significantly larger stream-to-stream heat transfer area as well as increased resistance to axial heat transfer.

As shown in Figs. 7 and 8, the numerical model predicted effectiveness was within the experimentally measured effectiveness uncertainty range for almost all of the data points. The data obtained at the lowest flow rates disagree with the model predictions. At low flow rates, the effectiveness is very sensitive to parasitic heat loads due to the low capacity rates of the two fluid streams. The model is in good agreement with the experimental data when the heat exchanger is being operated at design conditions (i.e., peak effectiveness).

The 43 die heat exchanger contains 5 dies with at least one functional integrated PRT (note that some plates were capable of measuring the temperature on only one fluid). Prior to testing but after assembly, the integrated PRTs were calibrated against commercially calibrated PRTs that were installed in the heat exchanger headers at each fluid inlet and outlet. The estimated uncertainty of the integrated PRTs is ±1.0 K [16]. The integrated PRTs provide a measurement

of the temperature distribution associated with each test point. The measured temperature distribution (the hot and cold fluid temperatures as a function of axial position, expressed in terms of the plate number) associated with the lowest mass flow rate data point in Fig. 8 is shown in Fig. 9. Also shown in Fig. 9 are the hot and cold temperatures predicted by the numerical model for the same inlet conditions.

The measured heat exchanger temperature distribution for the highest mass flow rate data point shown in Fig. 8 is presented in Fig. 10. Also presented in Fig. 10 is the temperature distribution predicted by the numerical model for the same inlet conditions.

The fidelity of the model was verified by carrying out an additional set of tests using ethane as the working fluid with the 43 die heat exchanger. The measured and predicted effectiveness based on the hot and cold fluids is shown in Fig. 11 as a function of mass flow rate. The warm inlet temperature was maintained between 295 K and 298 K while the cold inlet temperature was maintained between 242 K and 255 K. The numerical model slightly overpredicts the effectiveness but does correctly predict the mass flow rate at which the peak effectiveness is observed.

The temperature distributions for the lowest and highest ethane mass flow rate data points test are presented in Figs. 12 and 13, respectively. The temperature distribution measured using ethane exhibits the same behaviors observed using helium and discussed previously.

Examining Figs. 7–13 shows that the perforated plate heat exchanger model presented in this paper is in good agreement with the experimental data. This agreement is not only evident in the overall performance but also in the predicted and measured temperature distribution within the heat exchanger.

Axial conduction is the dominant effectiveness penalty at low mass flow rate operating conditions (i.e., high *NTU* and high λ conditions) and causes “temperature jumps” at the inlets to the heat exchanger [2]. This behavior is predicted by analytical and numerical models and causes the wall temperature at the ends of the heat exchanger to be strongly biased toward the outlet stream temperature. The stream-to-stream temperature difference is small (because the *NTU* is large) and the only thing preventing the heat exchanger from achieving an effectiveness near unity is the presence of the sharp temperature “jumps” at either end of the device. This behavior is shown clearly in Figs. 9 and 12 for the smallest helium and ethane mass flow rates, respectively.

When the mass flow rate is high, the dominant effectiveness penalty is related to the thermal resistance to heat transfer between the streams. This is consistent with a low *NTU*, low λ operating condition. The temperature difference between the streams becomes large and the temperature “jumps” at either end of the heat exchanger disappear. This behavior is shown clearly in Figs. 10 and 13 for the largest helium and ethane mass flow rates, respectively.

The effectiveness measurements shown in Figs. 8 and 11 also show the behavior expected for a heat exchanger experiencing an externally applied parasitic heat transfer. The parasitic heat transfer causes the heat transfer rate from the hot stream to be different than the heat transfer rate to the cold stream. In refrigeration applications, the parasitic heat transfer resulted in additional heating of the cold stream and reduced cooling of the hot stream. The parasitic heat loads associated with this experimental setup, radiation and conduction from the vacuum vessel, are strongly dependent on the cold end temperature of the heat exchanger but are almost completely independent of the mass flow rate through the heat exchanger. Thus the difference between the effectiveness associated with the hot and cold fluids is high when mass flow rate is small but becomes small as the mass flow rate increases.

Comparing the experimental and numerical model results for the two working fluids shows a trend. The helium results match each other within experimental uncertainty in almost all cases but the ethane experimental results are consistently slightly lower than the model results. The cause of this discrepancy is not understood.

5 Conclusion

A numerical modeling technique for perforated plate heat exchangers was presented. This numerical model allows each perforated plate to be modeled in detail but retains computational efficiency by using nodes that are exponentially concentrated near the edges of each perforated plate. The individual plate and spacer models are integrated using energy balances and solved using a commercial equation solving program. The numerical model was applied to a specific perforated plate/spacer geometry that was fabricated from silicon heat exchanger plates and glass spacers. The model predictions were validated against experimental measurements in a cryogenic, vacuum insulated test facility using two different working fluids. Although the numerical model was experimentally validated using only cryogenic temperature gases, the same approach could be used to model heat exchangers operating at higher temperatures or with liquids as the working fluid provided that suitable thermophysical property data and flow correlations are available.

Several of the perforated plates within the heat exchanger included integrated platinum resistance temperature detectors and therefore it was possible to resolve the internal temperature distribution. The numerical model predictions were in good agreement with both the measured effectiveness based on the heat transfer to either stream as well as the temperature distribution measured within the heat exchanger.

Acknowledgments

This work was funded through the University of Michigan by a grant from the National Institute of Health, Grant No. NIH/NINBS R33 EB003349-05.

NomenclatureGreek SymbolsSubscripts

$\dot{C}$	fluid capacitance rate
Δx	dimensional element width
ΔZ	dimensionless element width
i	fluid enthalpy
L	axial length
$\dot{m}$	mass flow rate
N	number of elements
NTU	number of transfer units
$\dot{q}$	heat transfer rate
R	thermal resistance
T	temperature
UA	stream-to-stream conductance
x	axial distance
Z	dimensionless axial distance

χ	dimensionless heat load
ε	heat exchanger effectiveness
γ	grid concentration factor
λ	axial conduction parameter
μ	dimensionless hot stream capacitance rate
ν	dimensionless cold stream capacitance rate
θ	dimensionless temperature

ac	axial conduction
c	cold stream
h	hot stream
i	element number
in	inlet
J	plate number
max	maximum
min	minimum
p	plate
sp	spacer
out	outlet
w	wall

References

1. McMahon HO, Bowen RJ, Bleyle GA. A Perforated Plate Heat Exchanger. Trans. ASME 1950;72:623–632.
2. Nellis, GF.; Klein, SA. Heat Transfer. New York: Cambridge University Press; 2009.
3. Swift WL, Zagarola MV, Nellis GF, McCormick JA, Sixsmith H, Gibbon JA. Development of Turbo-Brayton technology for Low Temperature Applications. Cryogenics 1999;39:989–995.
4. Jeheon, J.; Jeong, S. Cryogenic Heat Exchanger With Photo-Etched Mini-Perforated Plates Allowing Flow By-Pass; Proceedings of the ASME/JSME Summer Heat Transfer Conference; 2007. p. 503-508.
5. Venkatarathnam G, Sarangi G. Matrix Heat Exchangers and Their Application in Cryogenic Systems, Cryogenics. 1990;30:907–918.
6. Venkatarathnam G. Effectiveness-NTU Relationship in Perforated. Plate Heat Exchangers, Cryogenics 1996;36:235–241.
7. Kroeger, PG. Performance Degradation in High Effectiveness Heat Exchanger Due to Axial Conduction Effects. In: Fast, RW., editor. Advances in Cryogenic Engineering. Vol. Vol. 31. New York: Plenum; 1967. p. 363-372.
8. Nellis GF. A Heat Exchanger Model That Includes Axial Conduction, Parasitic Heat Loads, and Property Variations. Cryogenics 2003;43:523–538.
9. Barron RF. Effect of Heat Transfer From Ambient on Cryogenic Heat Exchanger Performance. Adv. Cryog. Eng 1984;29:265–272.
10. Chowdhury K, Sarangi S. Performance of Cryogenic Heat Exchangers With Heat Leak From the Surroundings. Adv. Cryog. Eng 1984;29:273–280.

11. Sarangi, S.; Barclay, JA. Cryogenic Process Equipment. New York: ASME; 1984. An Analysis of Compact Heat Exchanger Performance; p. 37-44.
12. Venkatarathnam G, Sarangi G. Analysis of Matrix Heat Exchanger Performance. ASME J. Heat Transfer 1991;113:830–837.
13. Ahuja V, Green R. Application of Matrix Heat Exchangers to Thermomechanical Exergy Recovery From Liquid Hydrogen, Cryogenics. 1998;38(9):857–867.
14. Hoch, DW.; Nellis, GF.; Meagher, NL.; Maddocks, JR.; Stephens, S. Development and Testing of a Multi-Plate Recuperative Heat Exchanger for Use in a Hybrid Cryocooler. In: Miller, SD.; Ross, RG., Jr, editors. Cryocoolers. Vol. Vol. 14. Annapolis, MA: ICC Press; 2007. p. 515-524.
15. Klein, SA. Engineering Equation Solver (EES). 2008. www.fchart.com, Version 8.120.
16. White, MJ. MS thesis. Madison, WI: University of Wisconsin-Madison; 2008. Performance of a MEMS Heat Exchanger for a Cryosurgical Probe.
17. Zhu W, White MJ, Nellis GF, Klein SA, Gianchandani YB. A Si/Glass Bulk Micromachined Cryogenic Heat Exchanger for High Heat Loads: Fabrication, Test, and Application Results. J. Microelectromech. Syst 2010;19(1):38–47. [PubMed: 20490284]
18. White, MJ.; Zhu, W.; Nellis, GF.; Klein, SA.; Gianchandani, YB. Cryocoolers. Vol. 15. Long Beach, CA: ICC Press; 2008. Performance of a MEMS Heat Exchanger for a Cryosurgical Probe.
19. Zhu, W.; White, MJ.; Hoch, DW.; Nellis, GF.; Klein, SA.; Gianchandani, YB. Two Approaches to Micromachining Si Heat Exchangers for Joule-Thomson Cryosurgical Probes. Proceedings of the IEEE MEMS; Kobe, Japan. 2007. p. 317-320.
20. Zhu, W.; White, MJ.; Hoch, DW.; Nellis, GF.; Klein, SA.; Gianchandani, YB. A Perforated Plated Stacked Si/Glass Heat Exchanger With In-Situ Temperature Sensing for Joule-Thomson Coolers. Proceedings of the IEEE MEMS; Tuscon, AZ. 2008. p. 844-847.
21. Hoch, DW.; Zhu, W.; Nellis, GF.; Schuetter, SD.; Klein, SA.; Gianchandani, YB. Cryocoolers. Vol. 14. Annapolis, MD: ICC Press; 2006. Progress Towards a Micromachined Heat Exchanger for a Cryosurgical Probe; p. 505-514.

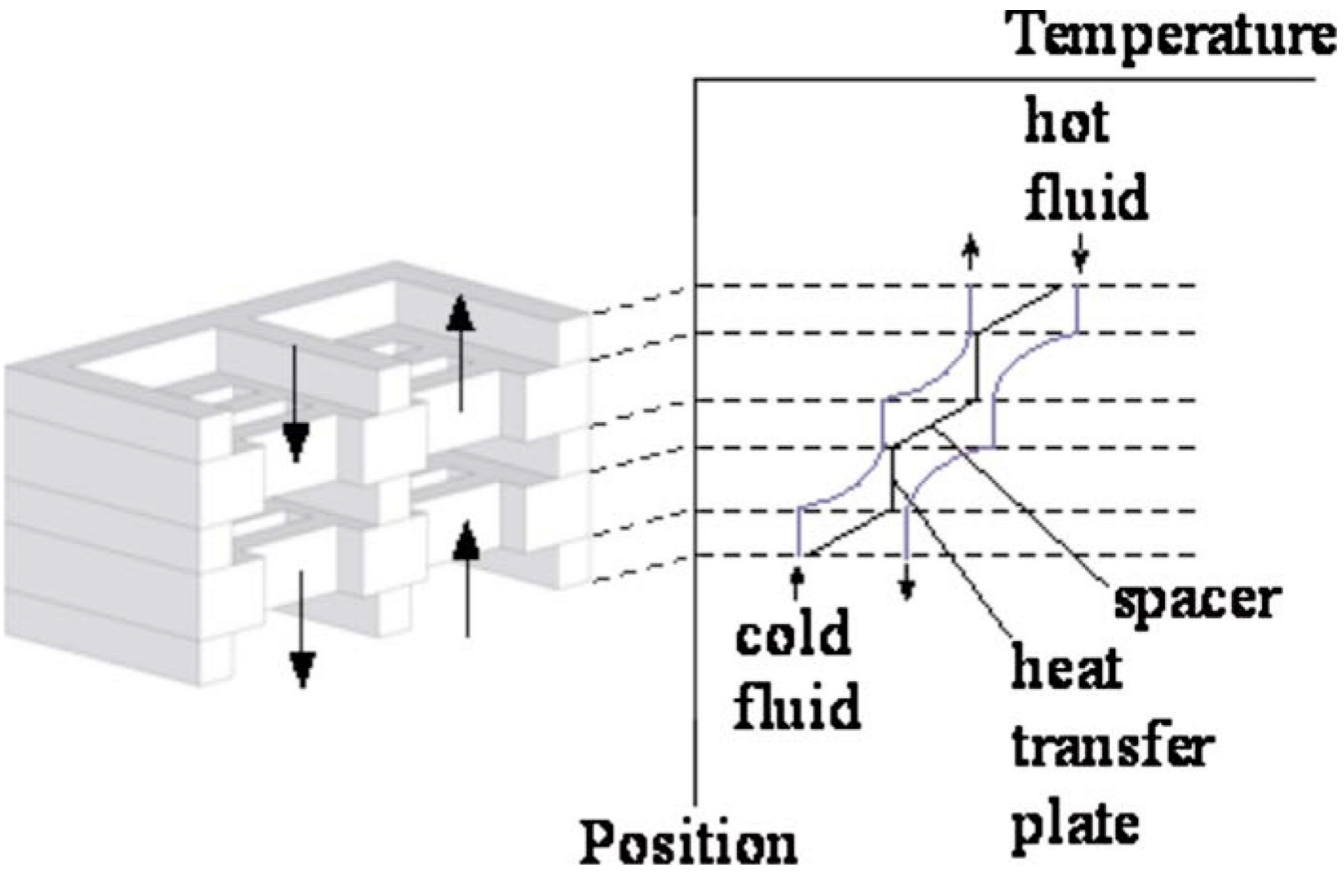

Fig. 1.
Qualitative temperature distribution in a spacer/heat transfer plate unit [2]

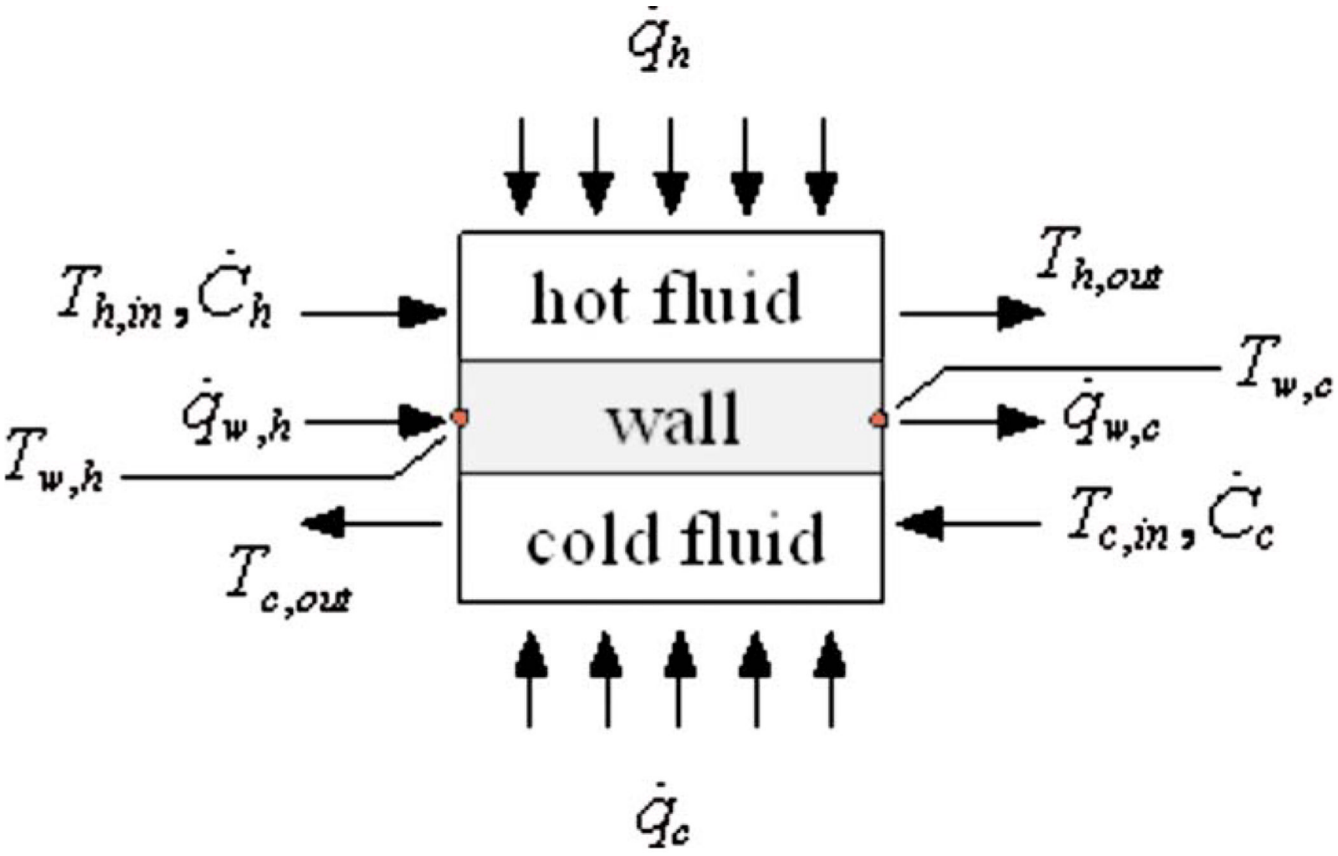

Fig. 2.
Schematic of a single plate

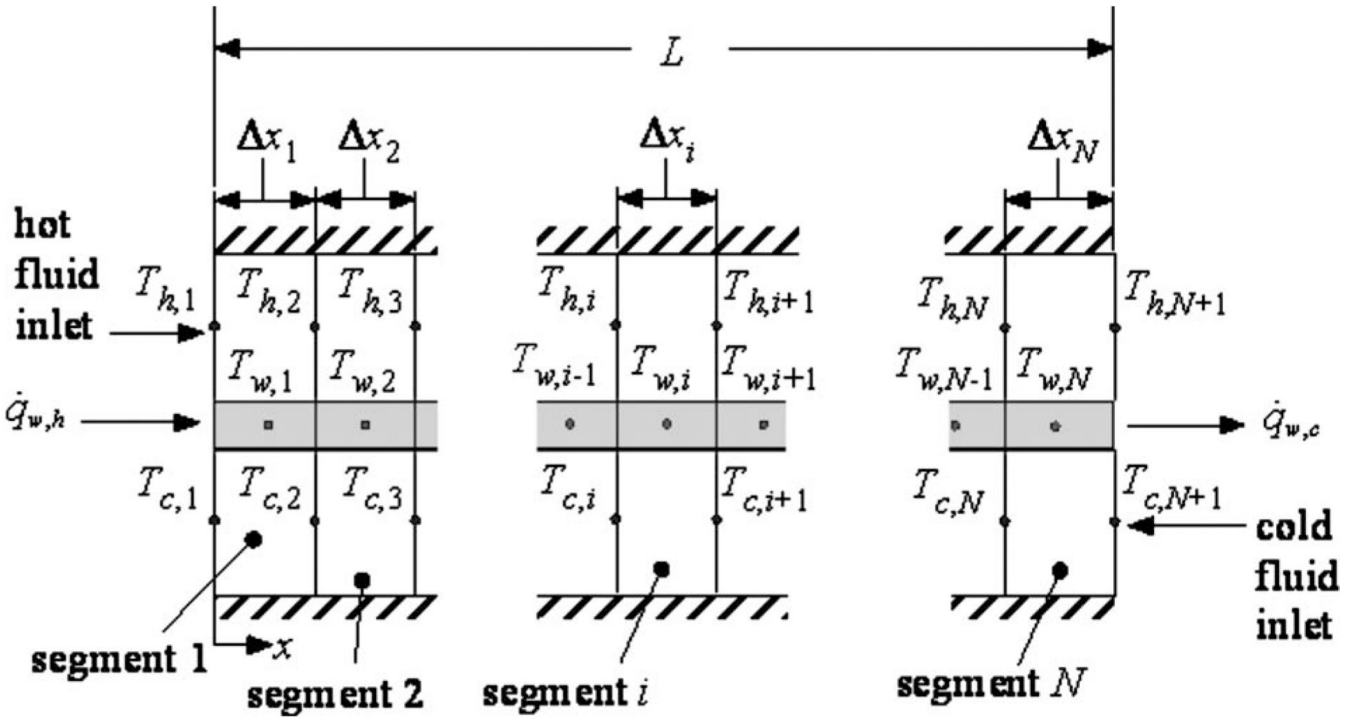

Fig. 3.
Distribution of the nodes used to simulate a single plate

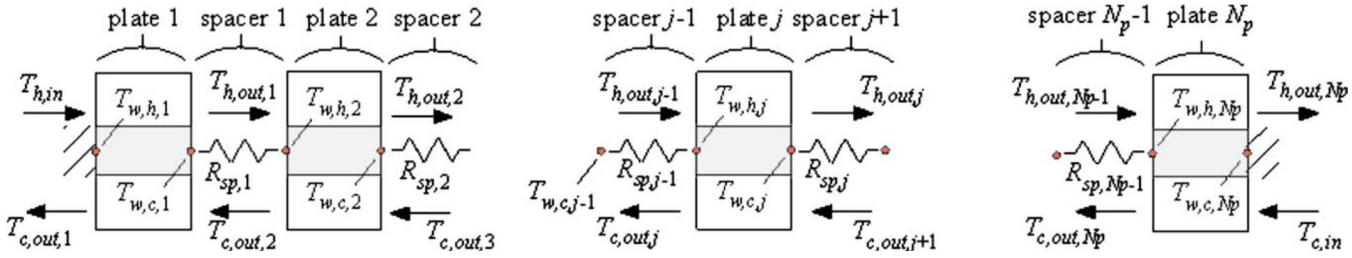

Fig. 4.
Integration of plates and spacers in order to simulate a perforated plate heat exchanger

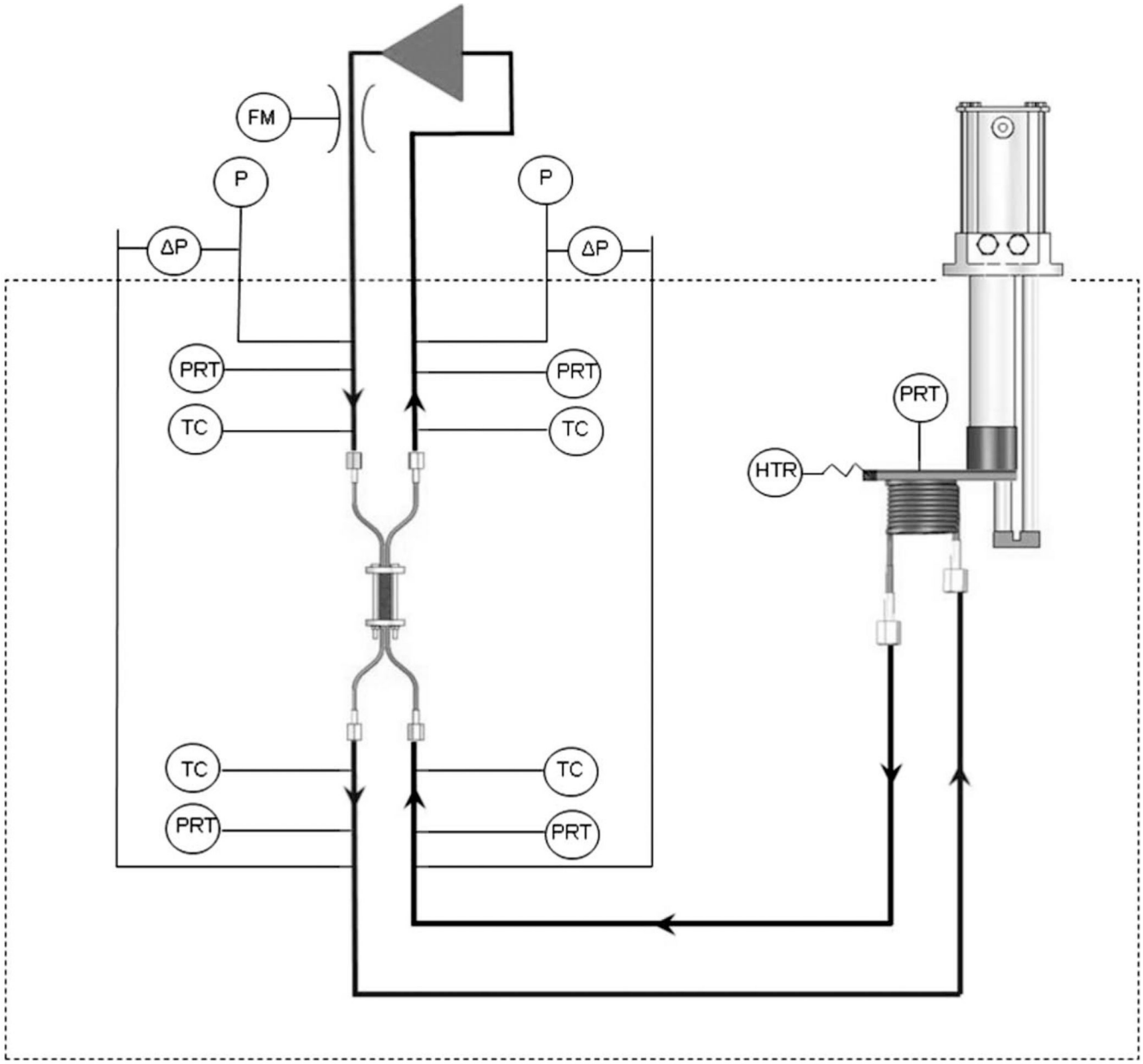

Fig. 5.

Simplified flow schematic of the cryogenic test facility used for testing the MEMS heat exchangers. The temperature at each port was measured using a platinum resistor (PRT) and a type E thermocouple (TC). The absolute pressure (P) was measured at the warm end ports of the heat exchanger and the differential pressure drop (ΔP) was measured on each side of the heat exchanger. A heater (HTR) was used to control the cryocooler temperature and a flow meter (FM) was used to measure the mass flow rate.

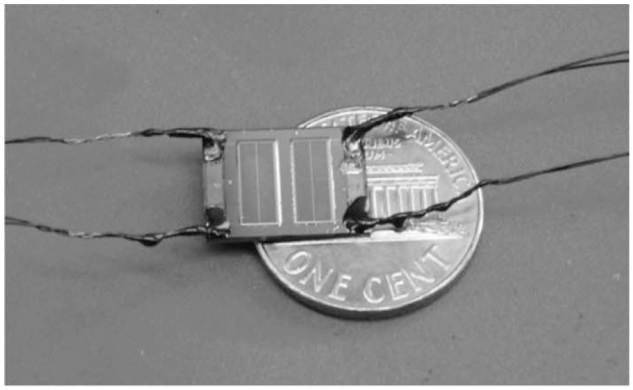

(*a*)

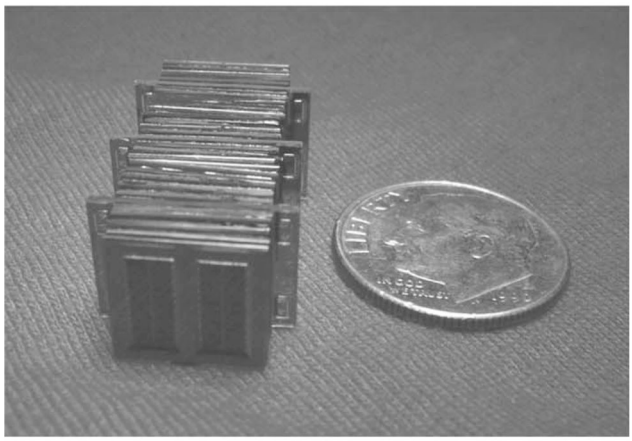

(*b*)

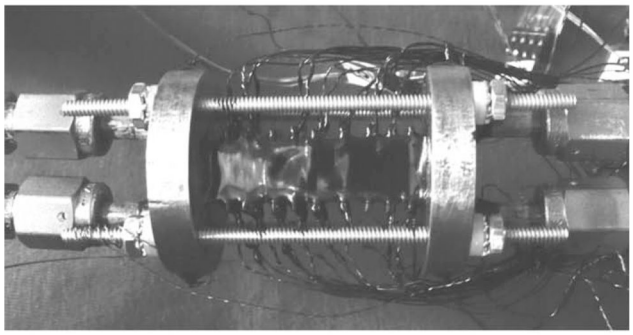

(*c*)

Fig. 6.
(*a*) Single die with integrated PRT, (*b*) perforated plate heat exchanger, and (*c*) perforated plate heat exchanger integrated with headers

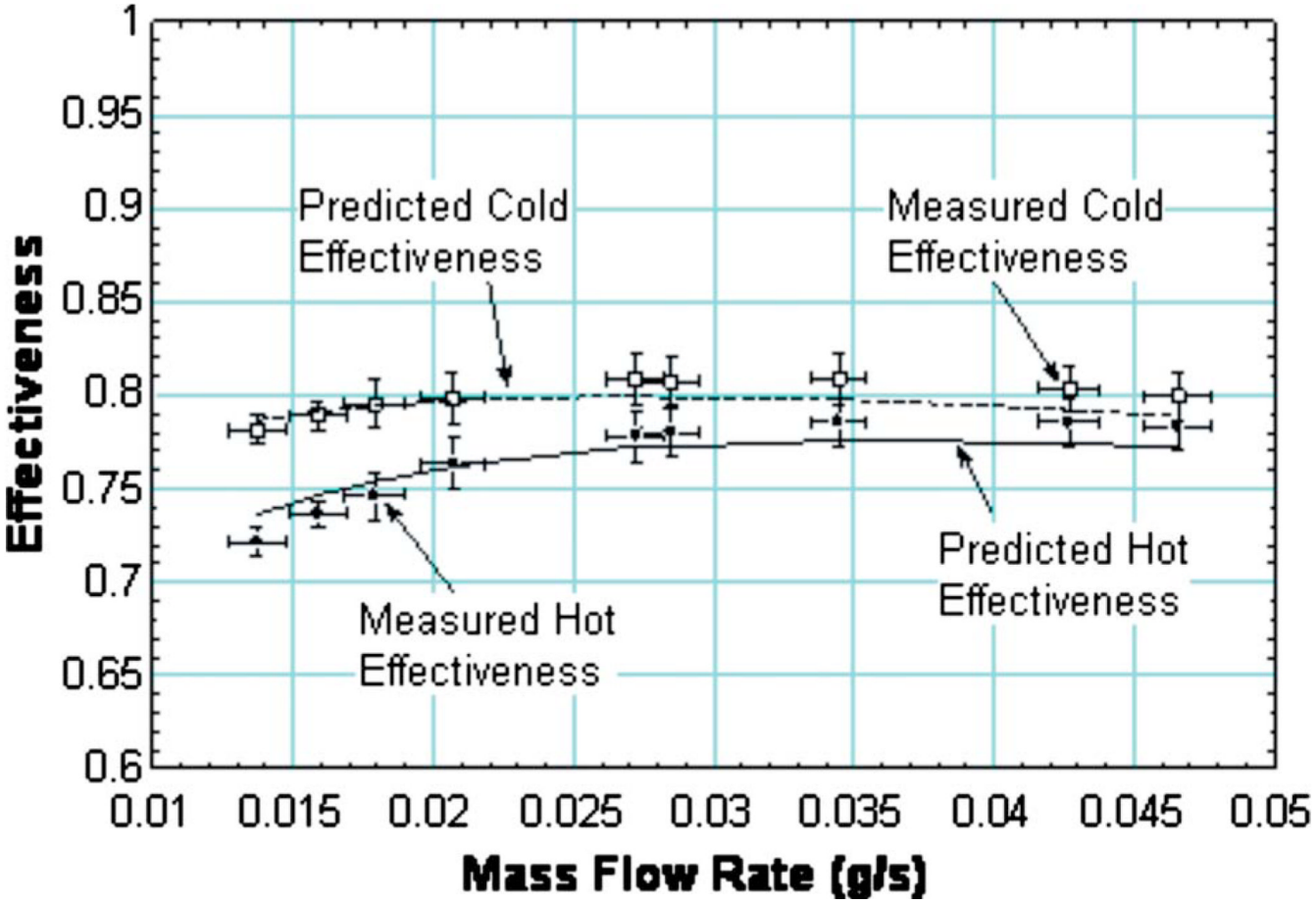

Fig. 7.
Measured and predicted effectiveness based on the hot and cold streams as a function of the mass flow rate for the 16 die heat exchanger tested with helium

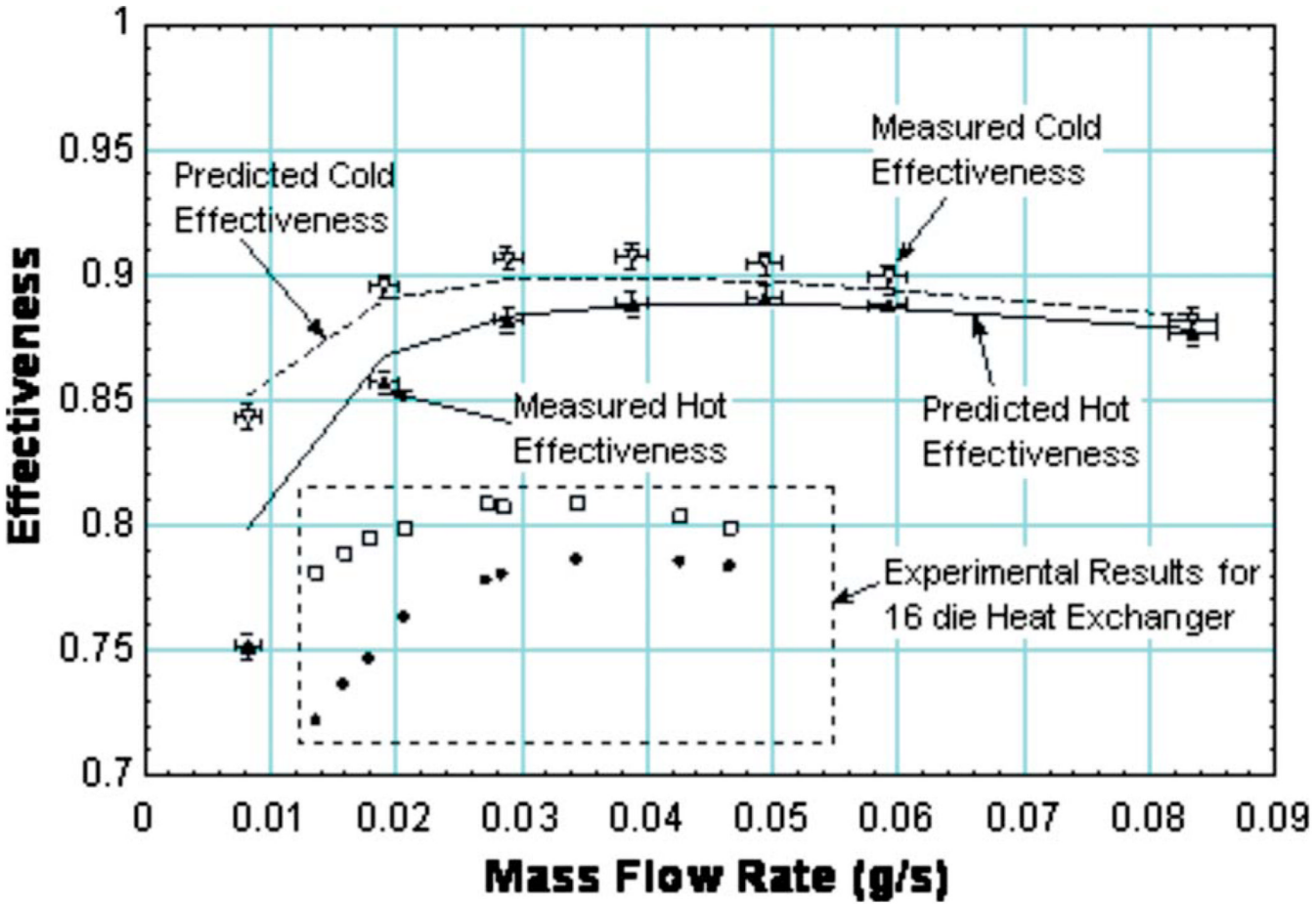

Fig. 8.

Measured and predicted effectiveness based on the hot and cold streams as a function of the mass flow rate for the 43 die heat exchanger tested with helium. Also shown are the test results for the 16 die heat exchanger, shown in Fig. 7.

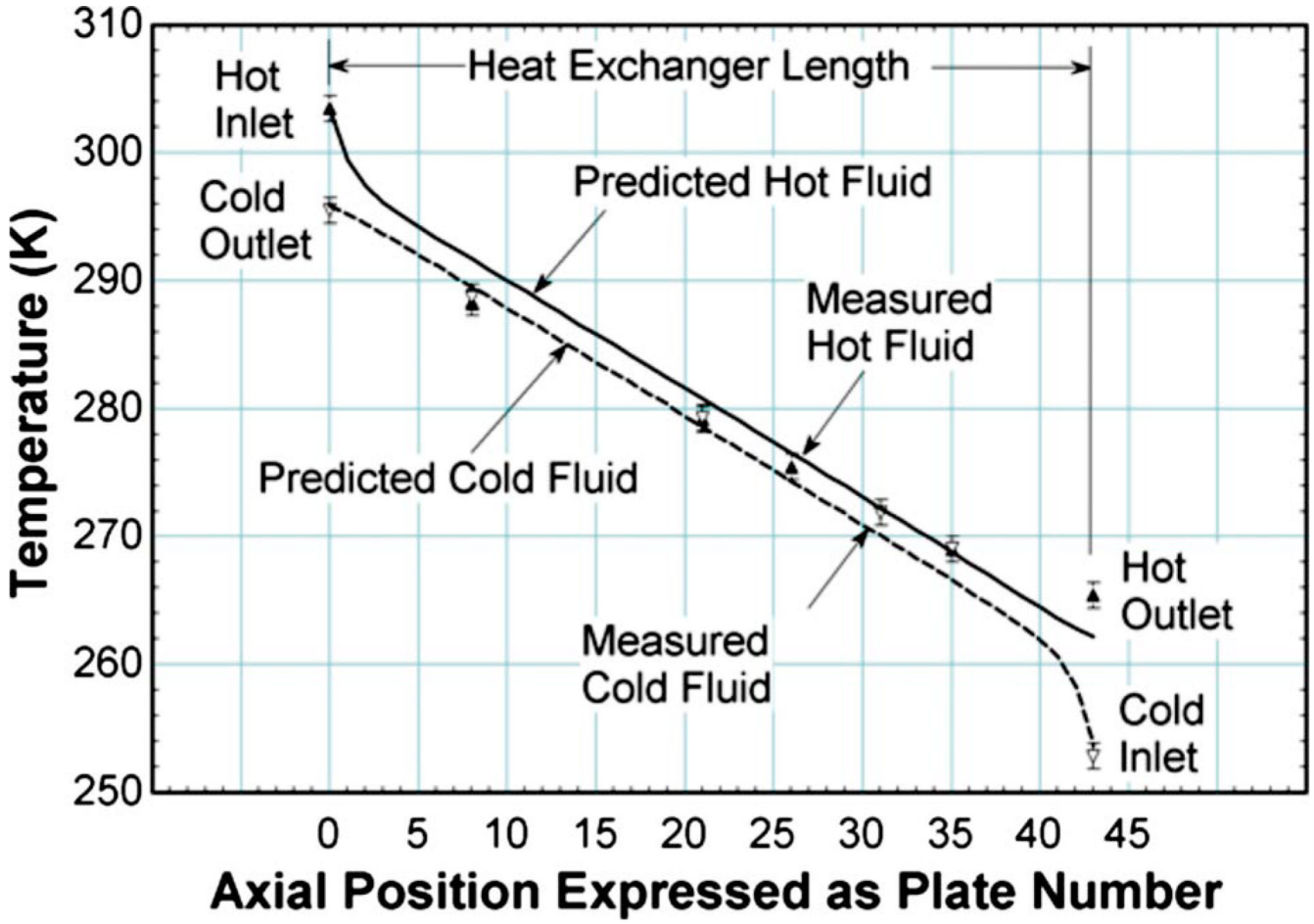

Fig. 9.

Measured and predicted hot and cold fluid temperatures as a function of position (expressed in terms of plate number) for the lowest mass flow rate data point taken with helium, shown in Fig. 8

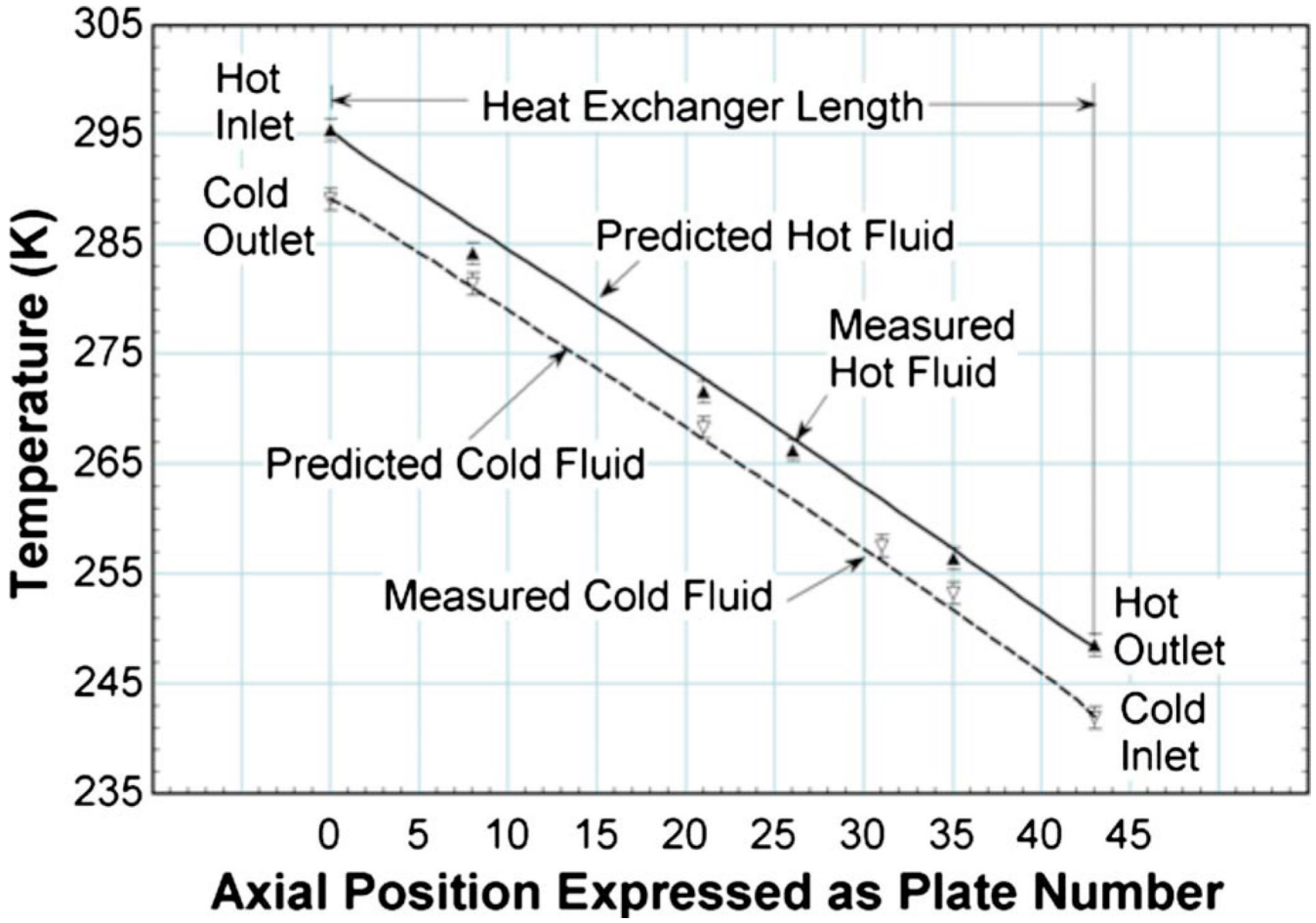

Fig. 10.
Measured and predicted hot and cold fluid temperatures as a function of position (expressed in terms of plate number) for the highest mass flow rate data point taken with helium, shown in Fig. 8

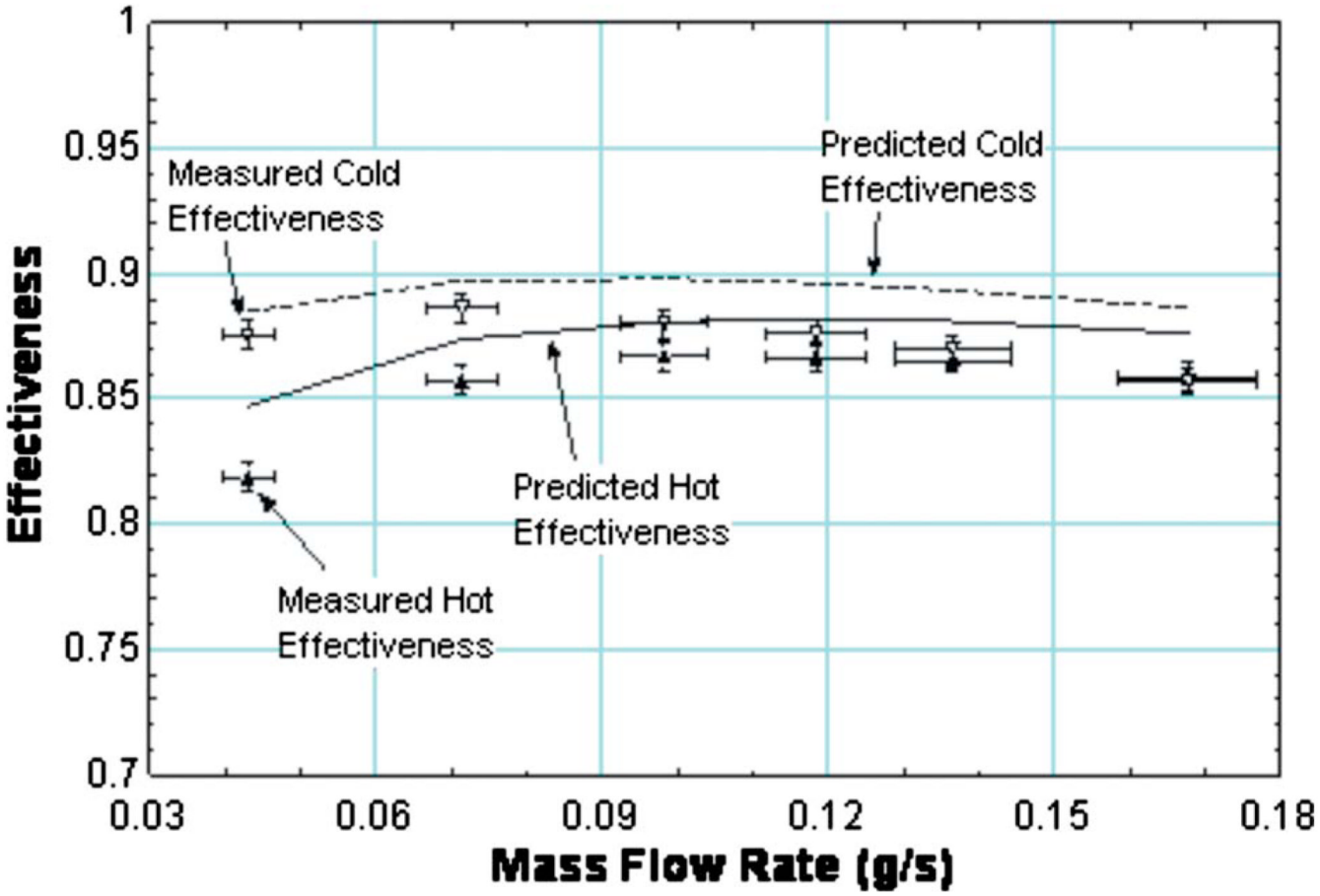

Fig. 11.
Measured and predicted effectiveness based on the hot and cold streams as a function of the mass flow rate for the 43 die heat exchanger tested with ethane

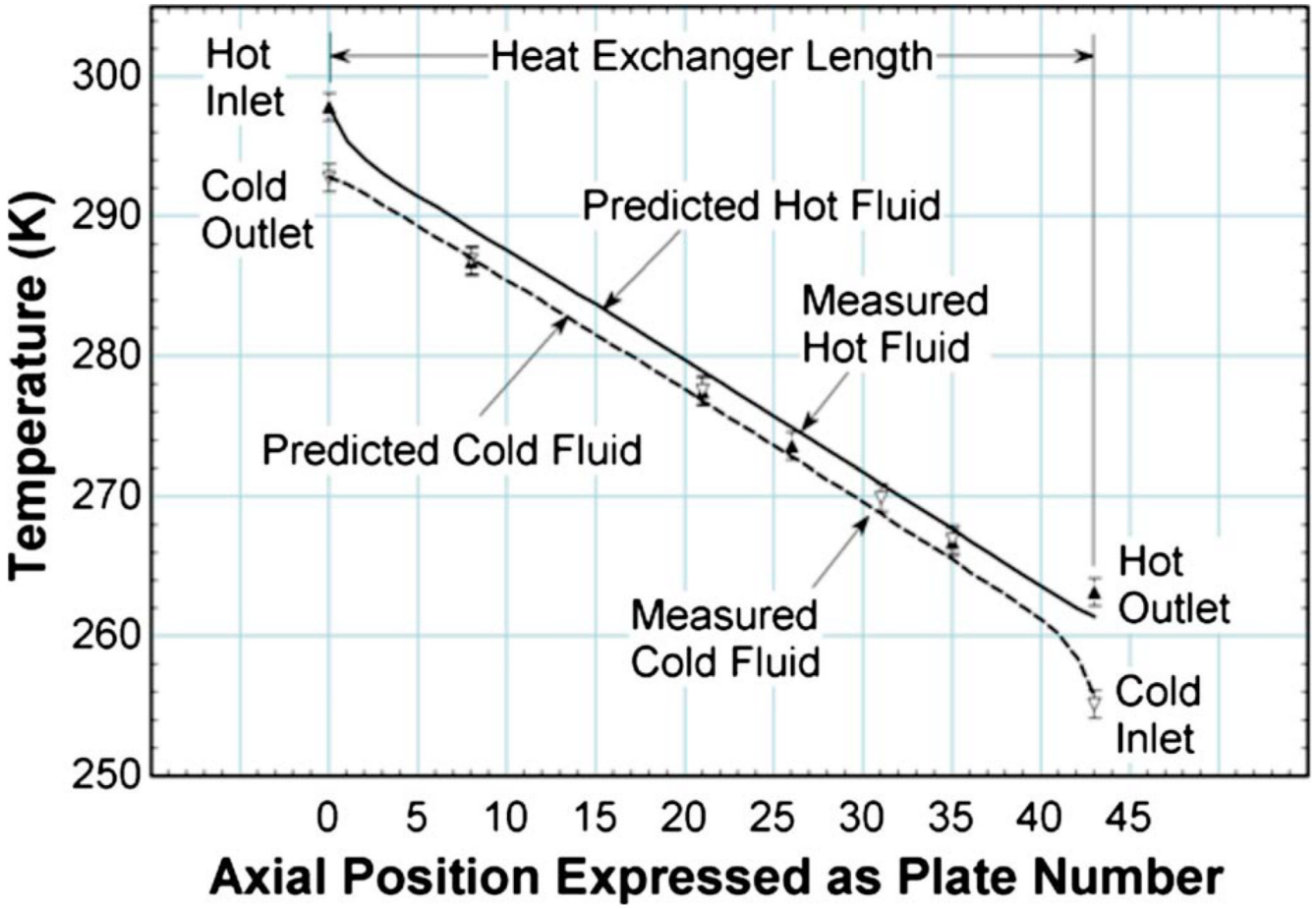

Fig. 12.

Measured and predicted hot and cold fluid temperatures as a function of position (expressed in terms of plate number) for the lowest mass flow rate data point taken with ethane, shown in Fig. 11

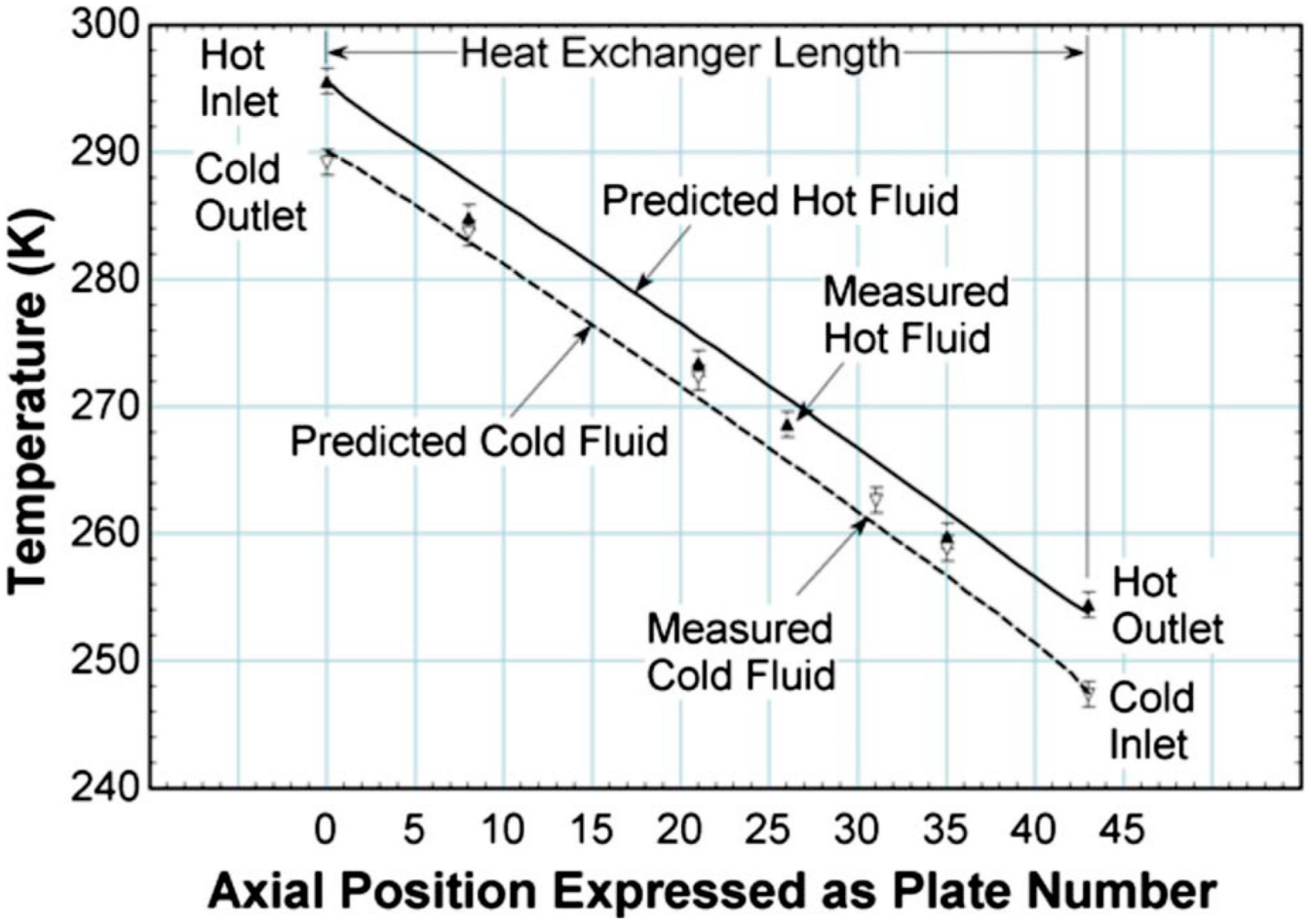

Fig. 13.
Measured and predicted hot and cold fluid temperatures as a function of position (expressed in terms of plate number) for the highest mass flow rate data point taken with ethane, shown in Fig. 11